THE UPPER-LEVEL STATIC STABILITY AND TROPOPAUSE STRUCTURE OF TROPICAL CYCLONES

by

Patrick Timothy Duran

A Dissertation

Submitted to the University at Albany, State University of New York

in Partial Fulfillment of

the Requirements for the Degree of

Doctor of Philosophy

College of Arts and Sciences

Department of Atmospheric and Environmental Sciences

2018

ABSTRACT

Upper-tropospheric thermodynamic processes can play an important role in tropical cyclone (TC) structure and evolution. Despite its importance, until recently few in-situ observations were available in the upper levels of TCs. Two recent field campaigns - the NASA Hurricane and Severe Storm Sentinel (HS3) and the Office of Naval Research Tropical Cyclone Intensity (TCI) experiment - provided a wealth of high-altitude observations within TCs. These observations revealed that the upper-level static stability and tropopause structure can change dramatically with both space and time in TCs.

The TCI dropsonde dataset collected during the rapid intensification (RI) of Hurricane Patricia (2015) revealed dramatic changes in tropopause height and temperature within the storm's inner core. These changes in tropopause structure were accompanied by a systematic decrease in tropopause-layer static stability over the eye. Outside of the eye, however, an initial decrease in static stability just above the tropopause was followed by an increase in static stability during the latter stages of RI.

Idealized simulations were conducted to examine the processes that might have been responsible for the tropopause variability observed in Hurricane Patricia. A static stability budget analysis revealed that three processes - differential advection, vertical gradients of radiative heating, and vertical gradients of turbulent mixing - can produce the observed variability. These results support the theoretical assumption that turbulent mixing plays a fundamental role in setting the upper-level potential temperature stratification in TCs. The existence of turbulence in the upper troposphere of TCs is corroborated by the presence of low-Richardson number layers in a large number of rawinsonde observations. These layers

were more common in hurricanes than in weaker TCs, as hurricanes were characterized by both smaller static static stability and larger vertical wind shear in the upper troposphere.

HS3 dropsondes deployed within and around TC Nadine (2012) observed two distinct upper-level stability maxima within the storm's cirrus canopy. Outside of the cirrus canopy, however, only one stability maximum was present in the upper levels. In a large rawinsonde dataset, multiple stability maxima like those observed in Nadine were observed more often within cold cirrus clouds than outside of cirrus. It is hypothesized that vertical gradients of radiative heating within cirrus clouds could produce these multiple stability maxima. MENTION THAT STABLE LAYER IS STRONGER WITHIN COLD CIRRUS AND THAT IT'S ALSO STRONGER IN HURRICANES THAN IN TD+TS?

ACKNOWLEDGEMENTS

This dissertation is the fulfillment of a childhood dream that would not have come true without the selfless dedication of countless people.

First I must thank my advisor, John Molinari, for his unswerving kindness, humility, and patience over these past six years. Former students have described him as a "brilliant scientist and an even better man," an assessment with which I wholeheartedly concur. I could not have asked for a better mentor, and am so grateful for the opportunities he has given to me.

I also would like to thank my committee members - Kristen Corbosiero, Robert Fovell, Brian Tang, and Ryan Torn - for their guidance and support over these years. Truly an academic all-star team, I will continue to look up to each of them as models of scientific brilliance.

Thanks to all of the DAES faculty for building and carefully maintaining such a positive and constructive departmental culture. It was always comforting to know that every faculty member truly cared about the students, and always worked to build us up as scientists and professionals. Nowhere was their dedication to students more evident than in their outstanding courses, which I thoroughly enjoyed, and which greatly contributed to my knowledge.

I also owe a tremendous debt to Steven Lazarus and Michael Splitt of the Florida Institute of Technology, whose selfless investment in me as an undergraduate played a critical role in my academic development, and prepared me for PhD-level research and course work.

I am grateful for the support and friendship of all of the DAES graduate students,

particularly Travis Elless, Stephanie Stevenson, Oscar Chimborazo, Sarah Ditchek, Matthew Vaughan, and Steven Fuhrman. Their friendship and encouragement over these years has meant a lot to me. I owe a special thanks to Chip Helms for not only being a fantastic friend, but for innumerable stimulating conversations, and for introducing me to so many people in the tropical meteorology community. Thanks also to research associate Dave Vollaro, whose guidance during my first year of graduate school greatly accelerated my development as a programmer, and whose baseball knowledge far surpassed mine.

Last and most importantly, I thank my fiancée, Erika Navarro, for her constant love and support, and my parents for the innumerable sacrifices that they have made on my behalf. Their gentle encouragement always pushed me to achieve my greatest potential, and their belief in me provided indispensible sustenance during times of hardship. This work is dedicated to them.

CONTENTS

1. Introduction

1.1 Section Heading

I can reference a section using the label, for example: Section 1.

1.1.1 Subsection Heading

2. The tropopause-layer static stability structure of tropical cyclones: Idealized modeling

2.1 Introduction

The preceding two chapters highlighted the effect of tropical cyclones on the tropopause and upper-level static stability structure in dropsonde observations. These observations alone, however, cannot explain the mechanisms that force the observed variability. Numerical simulations of an axisymmetric hurricane conducted in an idealized framework reproduced the observed variability. Using these simulations, some physical insight into these mechanisms is obtained and described in the present chapter.

2.2 Model Setup

The numerical simulations were performed using version 19.4 of Cloud Model 1 (CM1) described in Bryan and Rotunno (2009). The equations of motion were integrated on a 3000-km-wide, 30-km-deep axisymmetric grid with 1-km horizontal and 250-m vertical grid spacing. The computations were performed on an f-plane at 15°N latitude, over a sea surface with constant temperature of 30.5°C, which matches that observed near Hurricane Patricia (2015; Kimberlain et al. 2016). Horizontal turbulence was parameterized using the Smagorinsky scheme described in Bryan and Rotunno (2009, pg. 1773), with a prescribed mixing length that varied linearly from 100 m at a surface pressure of 1015 hPa to 1000 m at a surface pressure of 900 hPa. Vertical turbulence was parameterized using the formulation of Markowski and Bryan (2016, their Eq. 6), using an asymptotic vertical mixing length of 100 m. A Rayleigh damping layer was applied outside of the 2900-km radius and above the 25-km level to prevent spurious gravity wave reflection at the model boundaries. Microphysical processes were parameterized using the Thompson et al. (2004) scheme and radiative heating tendencies were computed every two minutes using the Rapid Radiative Transfer Model for GCMs (RRTMG) longwave and shortwave schemes (Iacono et al. 2008). The initial

temperature and humidity field was horizontally homogeneous and determined by averaging all Climate Forecast System Reanalysis (CFSR) grid points within 100 km of Patricia's center of circulation at 18 UTC 21 October 2015. The vortex described in Rotunno and Emanuel (1987, their Eq. 37) was used to initialize the wind field, setting all parameters equal to the values used therein.

Although hurricanes simulated in an axisymmetric framework tend to be more intense than those observed in nature, the intensity evolution of this simulation matches reasonably well with that observed in Hurricane Patricia. After an initial spin-up period of about 20 hours, the modeled storm (Fig. 2.1, blue lines) began an RI period that lasted approximately 30 hours. After this RI, the storm continued to intensify more slowly until the maximum 10-m wind speed reached 89 m s^{-1} and the sea-level pressure reached its minimum of 846 hPa 81 hours into the simulation. Hurricane Patricia (red stars) exhibited a similar intensity evolution prior to its landfall, with an RI period leading to a maximum 10-m wind speed of 95 m s^{-1} and a minimum sea-level pressure of 872 hPa.

2.3 Budget Computation

The static stability can be expressed as the squared Brunt-Väisälä frequency:

$$N_m^2 = \frac{g}{T}\left(\frac{\partial T}{\partial z} + \Gamma_m\right)\left(1 + \frac{T}{R_d/R_v + q_s}\frac{\partial q_s}{\partial T}\right) - \frac{g}{1+q_t}\frac{\partial q_t}{\partial z}, \tag{2.1}$$

where g is gravitational acceleration, T is temperature, R_d and R_v are the gas constants of dry air and water vapor, respectively, q_s is the saturation mixing ratio, q_t is the total condensate mixing ratio, and Γ_m is the moist-adiabatic lapse rate:

$$\Gamma_m = g(1+q_t)\left(\frac{1 + L_v q_s/R_d T}{c_{pm} + L_v \partial q_s/\partial T}\right), \tag{2.2}$$

where L_v is the latent heat of vaporization and c_{pm} is the specific heat of moist air at constant pressure. In the tropopause layer, q_s, $\partial q_s/\partial T$, and $\partial q_t/\partial z$ approach zero. In this limiting

case, Eq. 2.1 reduces to:

$$N^2 = \frac{g}{\theta}\frac{\partial \theta}{\partial z}, \tag{2.3}$$

where θ is the potential temperature.

To compute N^2, CM1 uses Eq. 2.1 in saturated environments and Eq. 2.3 in sub-saturated environments. For simplicity, however, only Eq. 2.3 will be employed for the budget computations throughout the entire domain[1].

Taking the time derivative of Eq. 2.3 yields the static stability tendency:

$$\frac{\partial N^2}{\partial t} = \frac{g}{\theta}\frac{\partial}{\partial z}\frac{\partial \theta}{\partial t} - \frac{g}{\theta^2}\frac{\partial \theta}{\partial z}\frac{\partial \theta}{\partial t}, \tag{2.4}$$

where the potential temperature tendency, $\partial\theta/\partial t$, can be written, following Bryan (cited 2018):

$$\frac{\partial \theta}{\partial t} = -u\frac{\partial \theta}{\partial r} - w\frac{\partial \theta}{\partial z} + HTURB + VTURB + MP + RAD + DISS \tag{2.5}$$

Each term on the right-hand side of Eq. 2.5 represents a θ budget variable, each of which is output directly by the model every minute.

The first term on the right-hand side of Eq. 2.4 is larger than the second term throughout most of the tropopause layer (not shown). Consequently, the contribution of each of the terms in Eq. 2.5 to the N^2 tendency can be interpreted in light of a vertical gradient of each term.

Taking the vertical gradient of the first two terms on the right-hand side of Eq. 2.5 yields the time tendency of the vertical θ gradient due to horizontal and vertical advection[2]:

$$\left(\frac{\partial}{\partial t}\frac{\partial \theta}{\partial z}\right)_{adv} = -u\frac{\partial}{\partial r}\frac{\partial \theta}{\partial z} - w\frac{\partial}{\partial z}\frac{\partial \theta}{\partial z} - \frac{\partial u}{\partial z}\frac{\partial \theta}{\partial r} - \frac{\partial w}{\partial z}\frac{\partial \theta}{\partial z}. \tag{2.6}$$

The first two terms on the right-hand side of Eq. 2.6 represent advection of static stability by

[1] The validity of this approximation will be substantiated later in this section.

[2] These terms include the tendencies due to implicit diffusion in the fifth-order finite differencing scheme, which are separated from the advection terms in the CM1 version 19.4 budget output.

the radial and vertical wind, respectively. These terms act to rearrange the static stability field, but cannot strengthen or weaken static stability maxima or minima. The third and fourth terms on the right-hand side of Eq. 2.6 represent, respectively, the tilting of isentropes in the presence of vertical wind shear, and the stretching or squashing of isentropes by vertical gradients of vertical velocity. Since these terms involve velocity gradients, they can act to strengthen or weaken static stability maxima or minima through differential advection. Unless otherwise stated, any reference to "advection" in this paper indicates the sum of all of the terms in Eq. 2.6.

Returning to Eq. 2.5, HTURB and VTURB are the θ tendencies from the horizontal and vertical turbulence parameterizations, MP is the tendency from the microphysics scheme, RAD is the tendency from the radiation scheme, and DISS is the tendency due to turbulent dissipation. This equation neglects Rayleigh damping, since the entire analysis domain lies outside of the regions where damping is applied. Each term in Eq. 2.5 is substituted for $\partial\theta/\partial t$ in Eq. 2.4, yielding the contribution of each budget term to the static stability tendency. These terms are summed, yielding an instantaneous "budget change" in N^2 every minute. The budget changes are then averaged over 24-hour periods and compared to the total model change in N^2 over that same time period, i.e.:

$$\Delta N^2_{budget} = \frac{1}{\delta t} \sum_{t=t_0}^{t_0+\delta t} \left. \frac{\partial N^2}{\partial t} \right|_t \tag{2.7}$$

$$\Delta N^2_{model} = N^2_{t_0+\delta t} - N^2_{t_0} \tag{2.8}$$

$$Residual = \Delta N^2_{model} - \Delta N^2_{budget} \tag{2.9}$$

where t_0 is an initial time and δt is 24 hours.

Eqs. 2.7-2.9 are plotted for three consecutive 24-hour periods in Fig. 2.2. For this and all subsequent radial-vertical cross sections, a 1-2-1 smoother is applied once in the radial direction to eliminate $2\Delta r$ noise that appears in some of the raw model output and calculated

fields. The left column of Fig. 2.2 depicts the model changes computed using Eq. 2.8, together with Eq. 2.1 in saturated environments and Eq. 2.3 in subsaturated environments. The center column depicts the budget changes computed using Eq. 2.7 together with Eq. 2.3 throughout the entire domain. Thus, the left column includes the effect of moisture in the N^2 computations, whereas the center column neglects moisture. The right column depicts the residuals, computed using Eq. 2.9 (i.e. the left column minus the center column.) In every 24-hour period, the budget changes are nearly identical to the model changes, which is reflected in the near-zero residuals in the right column. This indicates that the budget accurately represents the model variability, which implies that the neglect of moisture in the budget computation introduces negligible error within the analysis domain[3].

In the tropopause layer, some of the budget terms are small enough to be ignored. To determine which of the budget terms are most important, a time series of the contribution of each of the budget terms in Eq. 2.5 to the tropopause-layer static stability tendency is plotted in Fig. 2.3. For this figure, each of the budget terms is computed using the method described in Section 3, except with 1-hour averaging intervals instead of 24-hour intervals. The absolute values of these tendencies are then averaged over the radius-height domain of the plots shown in Fig. 2.2 and plotted as a time series[4]. Advection (Fig. 2.3, red line) plays an important role in the mean tropopause-layer static stability tendency at all times, and vertical turbulence (Fig. 2.3, blue line) and radiation (Fig. 2.3, dark green line) also contribute significantly. The remaining three processes - horizontal turbulence, microphysics, and dissipative heating - are negligible everywhere outside of the eyewall, and do not play important roles in the mesoscale tropopause variability.

The preceding analysis indicates that, at all times, three budget terms dominate the

[3] This is not the case in the lower- and mid-troposphere, where the residual actually exceeds the budget tendencies in many places, likely due to the neglect of moisture; thus we limit this analysis to the upper troposphere and lower stratosphere.

[4] It will be seeen in subsequent figures that each of the terms contributes both positively and negatively to the N^2 tendency within the analysis domain. Thus, taking an average over the domain tends to wash out the positive and negative contributions. To circumvent this problem, the absolute value of each of the terms is averaged.

tropopause-layer static stability tendency: advection, vertical turbulence, and radiation. Variations in the magnitude and spatial structure of these terms drive the static stability changes depicted in Fig. 2.2; subsequent sections will focus on these variations and what causes them.

2.4 Results

2.4.1 Static stability evolution

The average N^2 over the first day of the simulation (Fig. 2.4a) indicates the presence of a weak N^2 maximum just above the cold-point tropopause. Over the subsequent 24 hours, during the RI period, the N^2 within and above this layer decreased within the 25-km radius (Fig. 2.4b). This decreasing N^2 corresponded to an increase in the tropopause height within the developing eye, maximized at the storm center. Outside of the eye, meanwhile, the tropopause height decreased over the eyewall region (25-60-km radius) and increased only slightly outside of the 60-km radius. In this outer region, the N^2 maximum just above the tropopause strengthened during RI. These trends continued as the storm's intensity leveled off in the 48-72-hour period (Fig. 2.4c). The tropopause height increased to nearly 21 km at the storm center and sloped sharply downward to 16.3 km on the inner edge of the eyewall, near the 30 km radius. Static stability outside of the eye, meanwhile, continued to increase just above the cold-point tropopause. This N^2 evolution closely follows that observed in Hurricane Patricia (2015; Duran and Molinari 2018, see their Fig. 4). The mechanisms that led to these N^2 changes will be investigated in the subsequent sections.

2.4.2 Static stability budget analysis

0-24 hours

The initial spin-up period was characterized by a steady increase of the maximum wind speed from 11 m s^{-1} to 22 m s^{-1} (Fig. 2.1a, blue line), an intensification rate that closely matched that of TC Patricia (Fig. 2.1a, red stars). The weakening of the lower-stratospheric static stability maximum during this period is reflected in the total N^2 budget change over

this time (Fig. 2.5a). The layer just above the cold-point tropopause was characterized by decreasing N^2 (purple shading), maximizing at the storm center. At and immediately below the tropopause, meanwhile, N^2 increased during this time period (green shading). Although these tendencies extended out to the 200-km radius, they were particularly pronounced at innermost radii. A comparison of the contributions of advection (Fig. 2.5b), vertical turbulence (Fig. 2.5c), and radiation (Fig. 2.5d) reveals that advection was the primary driver of the N^2 tendency during this period, acting to stabilize near and just below the tropopause and destabilize above. Although vertical turbulence acted in opposition to advection (i.e. it acted to stabilize regions that advection acted to destabilize), the magnitude of the advective tendencies was larger, particularly at the innermost radii. The sum of advection and vertical turbulence (Fig. 2.5e) almost exactly replicated the static stability tendencies above the tropopause. Radiative tendencies, meanwhile, (Fig. 2.5d) acted to destabilize the layer below about 16 km and stabilize the layer between 16 and 17 km. The sum of advection, vertical turbulence, and radiation (Fig. 2.5f) reproduced the total change in N^2 almost exactly.

24-48 hours

During the RI period, the maximum wind speed increased from 22 m s^{-1} to 80 m s^{-1} (Fig. 2.1a). Over this time, N^2 within the eye generally decreased above 16 km and increased below (Fig. 2.6a), with the destabilization above 16 km maximizing near the level of the mean cold-point tropopause. These tendencies at the innermost radii were driven almost entirely by advection (Fig. 2.6b). Vertical turbulence (Fig. 2.6c) and radiation (Fig. 2.6d) contributed negligibly to the static stability tendencies in this region.

Outside of the eye, the N^2 evolution exhibited alternating layers of positive and negative tendencies. Near and above 18 km existed an upward-sloping region of decreasing N^2 that extended out to the 180-km radius. In this region, neither vertical turbulence nor radiation exhibited negative N^2 tendencies; advection was the only forcing for this destabilization. Immediately below this layer, just above the cold-point tropopause, was a region

of increasing N^2 that sloped upward from 17 km near the 30-km radius to just below 18 km outside of the 100-km radius. Advection and vertical turbulence both contributed to this positive N^2 tendency, with advection playing an important role below about 17.5 km and and turbulence playing an important role above. The sum of advection and turbulence (Fig. 2.6e) reveals two separate regions of increasing N^2 in the 17-18-km layer rather than one contiguous region. The addition of radiation to these two terms, however, (Fig. 2.6f) provides the link between these two regions, indicating that radiation also plays a role in strengthening the stable layer just above the tropopause. In the 16-17-km layer, just below the cold-point tropopause, a horizontally-extensive layer of destabilization also was forced by a combination of advection, vertical turbulence, and radiation. The sum of advection and vertical turbulence accounts for only a portion of the decreasing N^2 in this layer, and actually indicates forcing for stabilization near the 50-km radius and outside of the 130-km radius. Radiative tendencies overcome this forcing for stabilization in both of these regions to produce the radially-extensive region of destabilization observed just below the tropopause.

The sum of advection, vertical turbulence, and radiation (Fig. 2.6f) once again closely follows the observed N^2 variability, except in the eyewall region, where the neglect of latent heating and horizontal turbulence introduces some differences.

48-72 hours

After the storm's maximum wind speed leveled off near 80 m s^{-1} (Fig. 2.1a), the magnitude of the static stability tendencies within the eye decreased to near zero (Fig. 2.7a). Outside of the eye, however, N^2 continued to decrease in the layer immediately sorrounding the tropopause and increase just above. The sum of advection and vertical turbulence (Fig. 2.7e) indicates that these two processes account for most of the destabilization near the tropopause and some of the stabilization near the 18-km altitude. Below the tropopause, however, these two terms provided strong forcing for stabilization that was not observed in the budget change (Fig. 2.7a). Radiation (Fig. 2.7d), which generally forced stabilization

above 17 km and destabilization below, balanced out this forcing for stabilization in the upper troposphere. In the eyewall region (30-80-km radius), advection and vertical turbulence combined to force destabilization in the 17-18-km layer (Fig. 2.7e), which was not observed in the budget change (Fig. 2.7a). Radiation provided strong forcing for stabilization, which outweighed this effect and produced net stabilization in a portion of this region. Outside of the 80-km radius, both advection (Fig. 2.7b) and vertical turbulence (Fig. 2.7c) provided forcing for stabilization near and just above the 18-km level. The sum of the two terms (Fig. 2.7e) indicates increasing N^2 near the 18-km level everywhere outside of the 80-km radius, but this stabilization is slightly weaker in the 90-120-km radial band than the observed value. The addition of radiation (Fig. 2.7f) provided the extra forcing for stabilization required to account for the observed increase in N^2. Outside of the 120-km radius, the region of radiative forcing for stabilization sloped downward, and the increase in N^2 observed near 18 km can be explained entirely by a combination of advection and vertical turbulence.

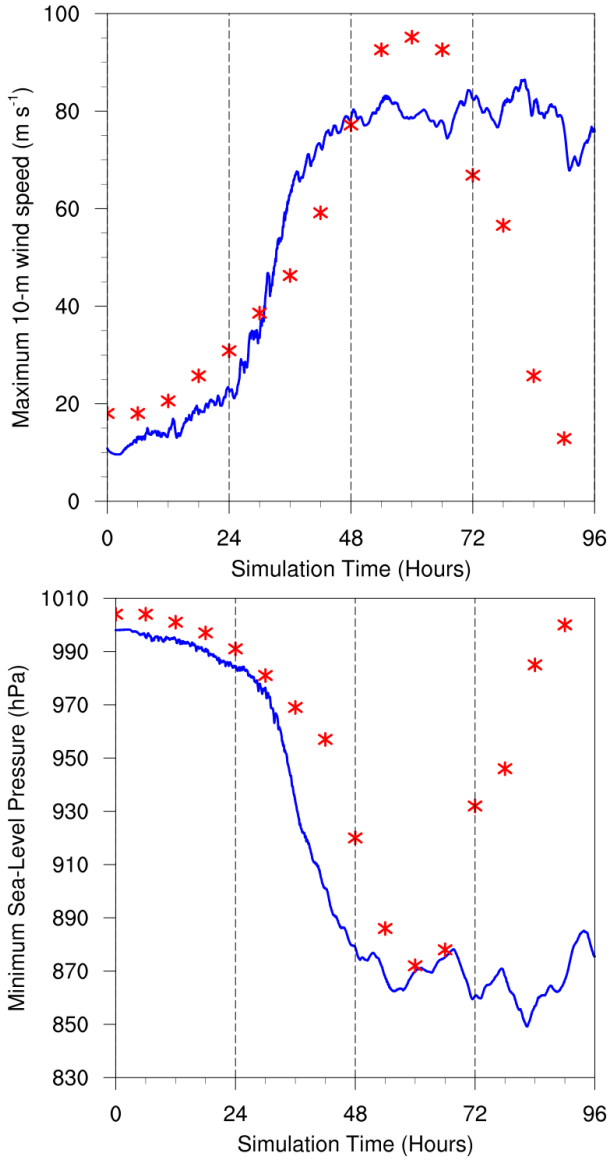

Figure 2.1: The maximum 10-m wind speed (top panel; m s^{-1}) and minimum sea-level pressure (bottom panel; hPa) in the simulated storm (blue lines; plotted every minute) and from Hurricane Patricia's best track (red stars; plotted every six hours beginning at the time Patricia attained tropical storm intensity). The rapid weakening during the later stage of Patricia's lifetime was induced by landfall.

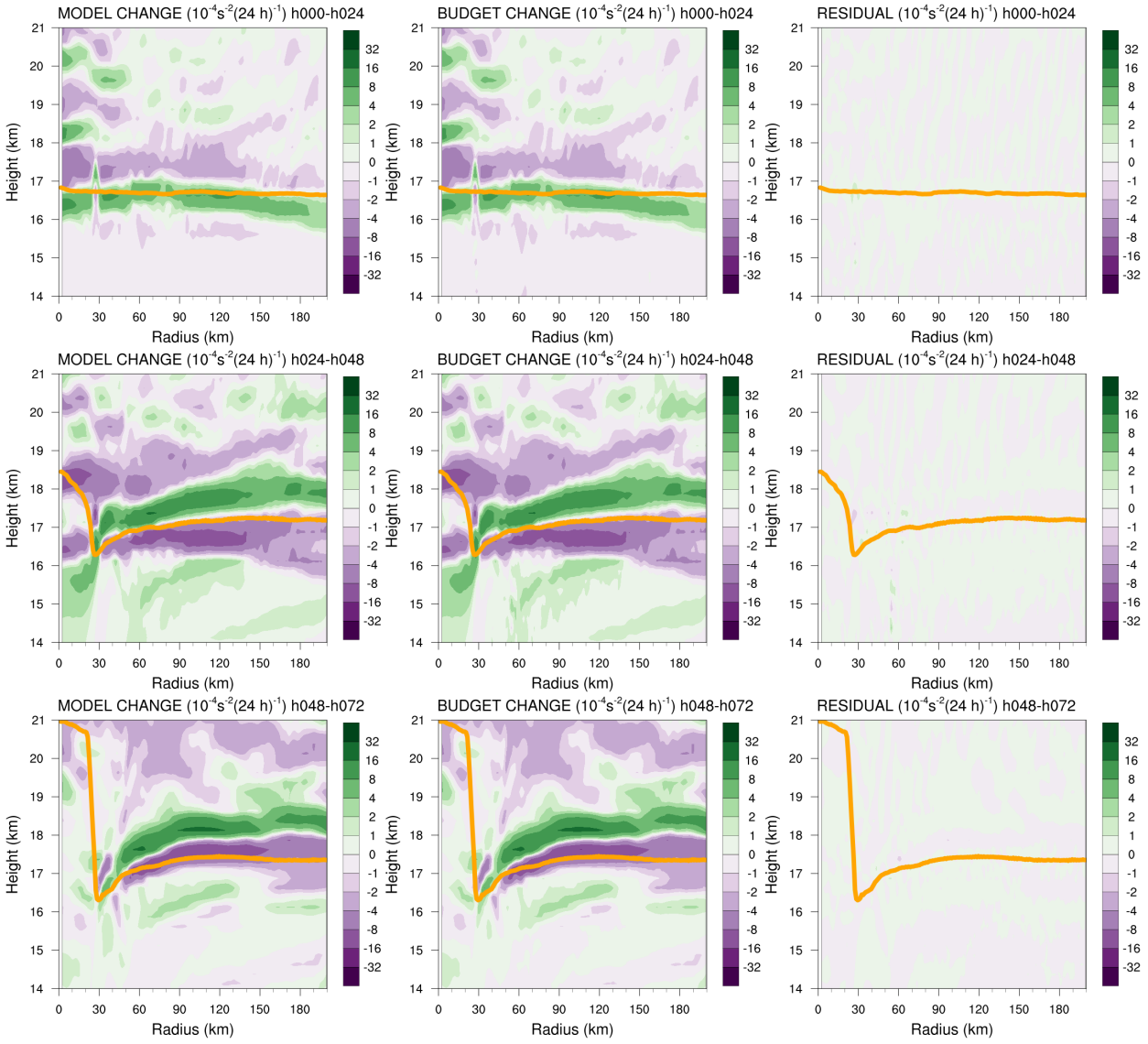

Figure 2.2: Left panels: Twenty-four-hour changes in squared Brunt-Väisälä frequency (N^2; 10^{-4} s^{-2}) computed using Eq. 2.8 over (top row) 0-24 hours, (middle row) 24-48 hours, (bottom row) 48-72 hours. Middle Panels: The N^2 change over the same time periods computed using Eqs. 2.4-2.7, Right Panels: The budget residual over the same time periods, computed by subtracting the budget change (middle column) from the model change (left column). Orange lines represent the cold-point tropopause height averaged over the same time periods.

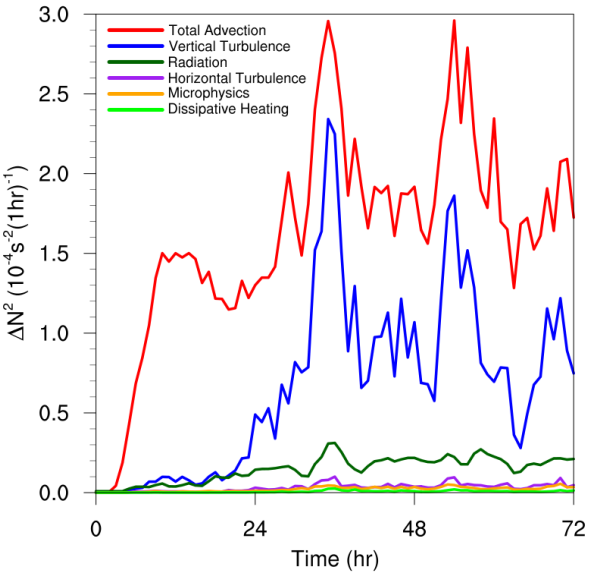

Figure 2.3: Time series of the contribution of each of the budget terms to the time tendency of the squared Brunt-Väisälä frequency (N^2; 10^{-4} s^{-2}). For each budget term, the absolute value of the N^2 tendency is averaged temporally over 1-hour periods (using output every minute), and spatially in a region extending from 0 to 200 km radius and 14 to 21 km altitude.

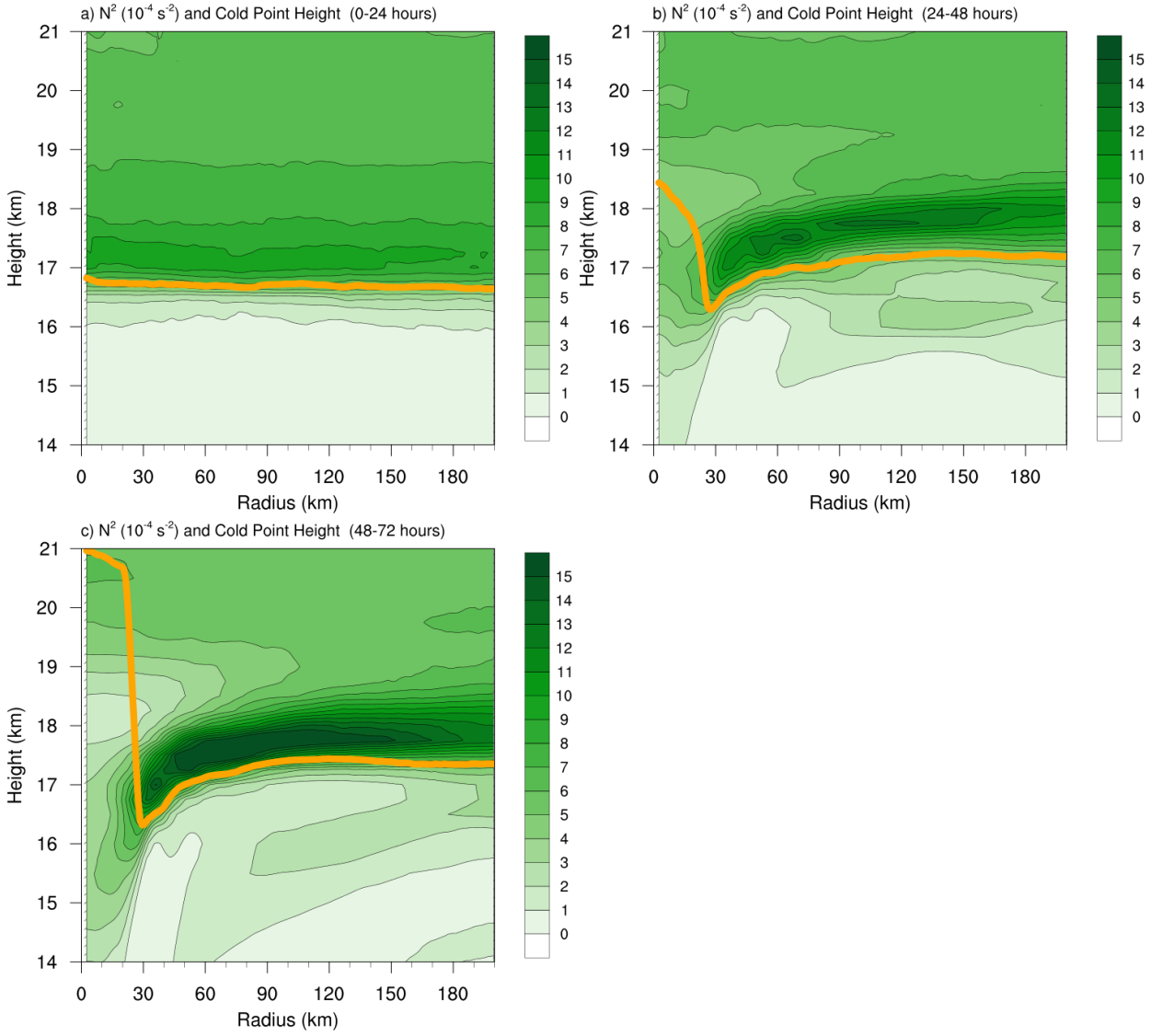

Figure 2.4: Twenty-four-hour averages of squared Brunt-Väisälä frequency (N^2; 10^{-4} s^{-2}) over (a) 0-24 hours, (b) 24-48 hours, (c) 48-72 hours. Orange lines represent the cold-point tropopause height averaged over the same time periods.

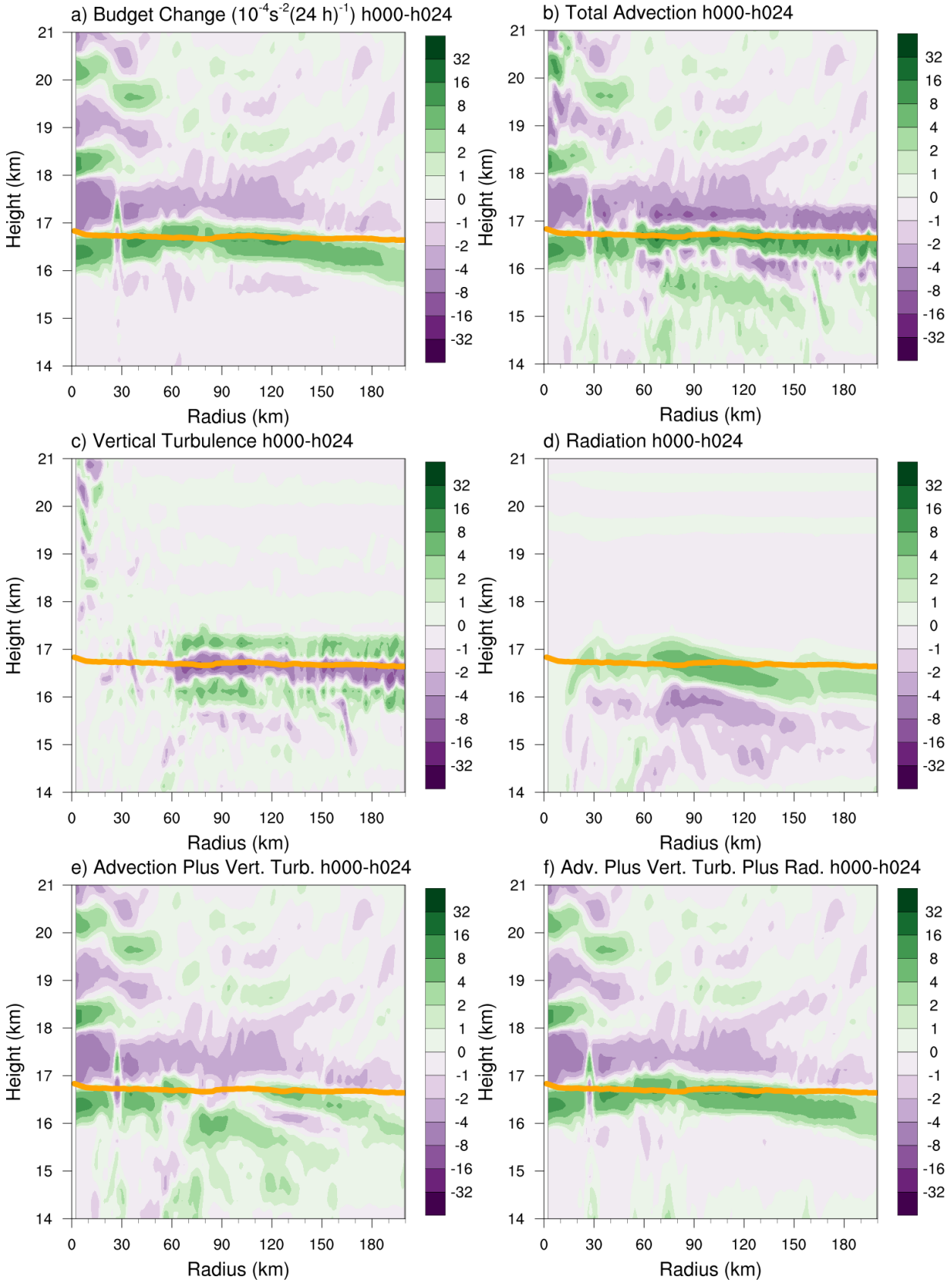
a) Budget Change ($10^{-4}s^{-2}(24\ h)^{-1}$) h000-h024
b) Total Advection h000-h024
c) Vertical Turbulence h000-h024
d) Radiation h000-h024
e) Advection Plus Vert. Turb. h000-h024
f) Adv. Plus Vert. Turb. Plus Rad. h000-h024
Height (km)
Radius (km)
21
20
19
18
17
16
15
14
0
30
60
90
120
150
180
32
16
8
4
2
1
0
-1
-2
-4
-8
-16
-32

Figure 2.5: (a) Total change in N^2 over the 0-24-hour period (10^{-4} s^{-2} $(24\ h)^{-1}$) and the contributions to that change from (b) the sum of horizontal and vertical advection, (c) vertical turbulence, (d) longwave and shortwave radiation, (e) the sum of horizontal advection, vertical advection, and vertical turbulence, and (f) the sum of horizontal advection, vertical advection, vertical turbulence, and longwave and shortwave radiation. Green shading indicates regions of stabilization and purple shading indicates regions of destabilization. Orange lines represent the cold-point tropopause height averaged over the 0-24-hour period.

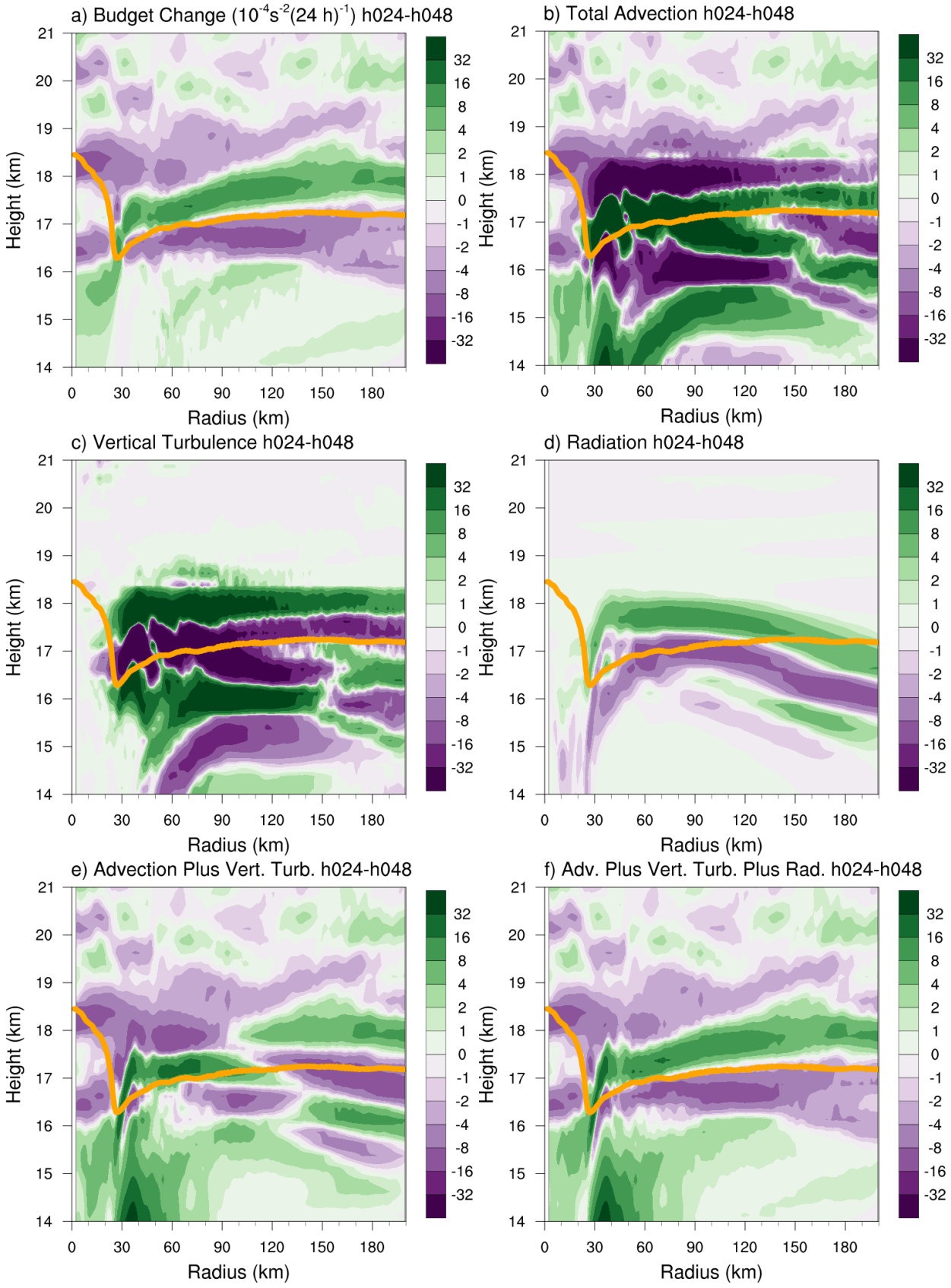

Figure 2.6: As in Fig. 2.5, but for the 24-48-hour period.

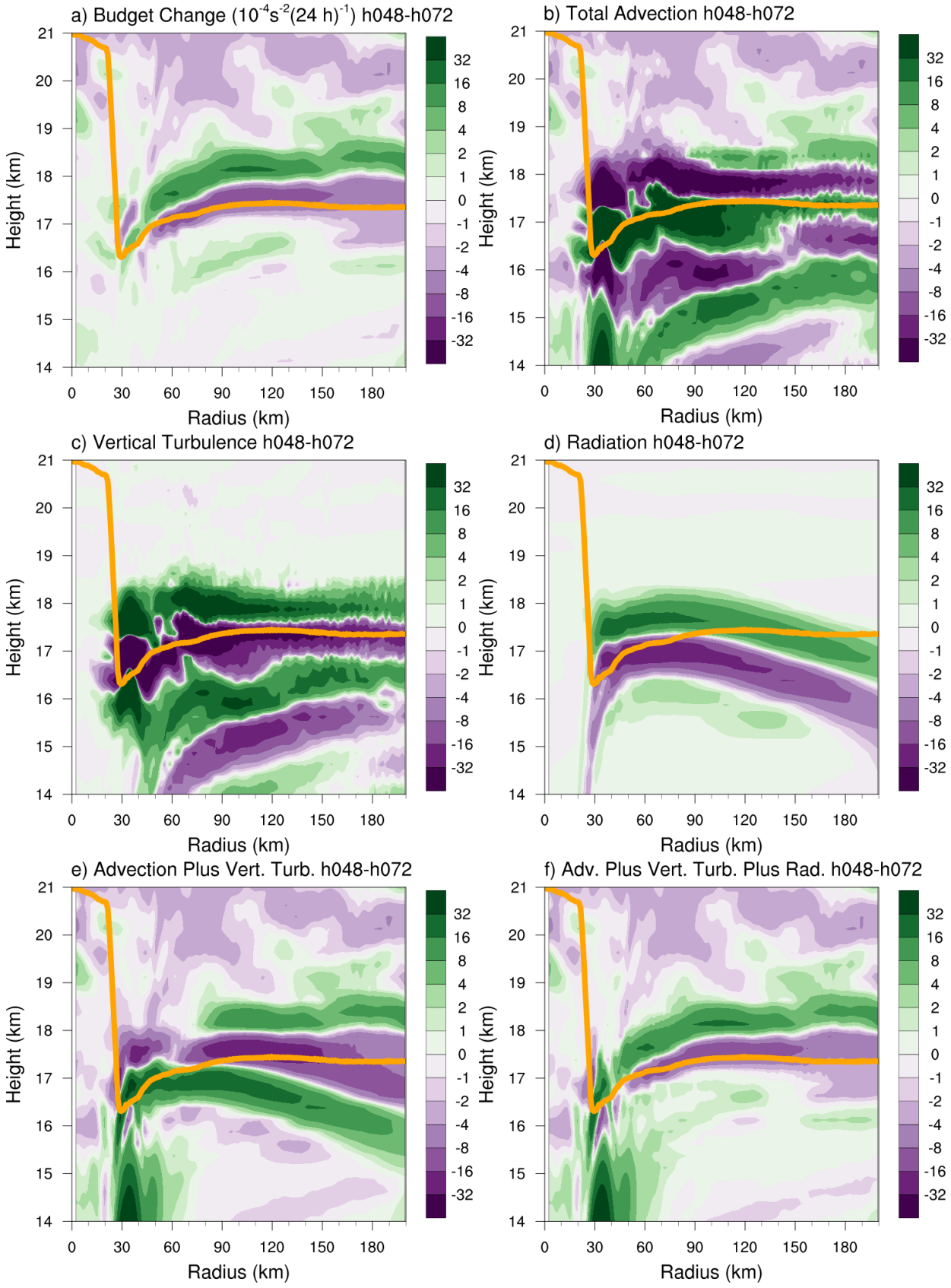

Figure 2.7: As in Fig. 2.5, but for the 48-72-hour period.

BIBLIOGRAPHY

Bryan, G. H., cited 2018: The governing equations for CM1. [Available online at http://www2.mmm.ucar.edu/people/bryan/cm1/cm1_equations.pdf].

Bryan, G. H., and R. Rotunno, 2009: The maximum intensity of tropical cyclones in axisymmetric numerical model simulations. *Mon. Wea. Rev.*, **137 (6)**, 1770–1789.

Duran, P., and J. Molinari, 2018: Dramatic inner-core tropopause variability during the rapid intensification of Hurricane Patricia (2015). *Mon. Wea. Rev.*, **146 (1)**, 119–134.

Iacono, M. J., J. S. Delamere, E. J. Mlawer, M. W. Shephard, S. A. Clough, and W. D. Collins, 2008: Radiative forcing by long-lived greenhouse gases: Calculations with the AER radiative transfer models. *J. Geophys. Res.*, **113 (D13103)**.

Kimberlain, T. B., E. S. Blake, and J. P. Cangialosi, 2016: Tropical cyclone report: Hurricane Patricia. National Hurricane Center. [Available online at www.nhc.noaa.gov].

Markowski, P. M., and G. H. Bryan, 2016: LES of laminar flow in the PBL: A potential problem for convective storm simulations. *Mon. Wea. Rev.*, **144**, 1841–1850.

Rotunno, R., and K. A. Emanuel, 1987: An air-sea interaction theory for tropical cyclones. Part II: Evolutionary study using a nonhydrostatic axisymmetric numerical model. *J. Atmos. Sci.*, **44**, 542–561.

Thompson, G., R. M. Rasmussen, and K. Manning, 2004: Explicit Forecasts of Winter Precipitation Using an Improved Bulk Microphysics Scheme. Part I: Description and Sensitivity Analysis. *Mon. Wea. Rev.*, **132 (2)**, 519–542.